



Linear disturbances in the rotating-disk flow: A comparison between results from simulations, experiments and theory



E. Appelquist^{a,*}, Shintaro Imayama^a, P. Henrik Alfredsson^{a,*}, P. Schlatter^a, R.J. Lingwood^{a,b}

^a Linné FLOW Centre, KTH Mechanics, Royal Institute of Technology, S-100 44 Stockholm, Sweden

^b Centre for Simulation and Applied Mechanics, School of Engineering and Materials Science, Queen Mary University of London, Mile End Road, London E1 4NS, UK

ARTICLE INFO

Article history:

Received 27 February 2015

Received in revised form

25 August 2015

Accepted 15 September 2015

Available online 6 November 2015

Keywords:

Linear stability theory

Direct numerical simulations

Hot-wire anemometry

Rotating-disk boundary layer

ABSTRACT

The incompressible Navier–Stokes equations have an exact similarity solution for the flow over an infinite rotating disk giving a laminar boundary layer of constant thickness, also known as the von Kármán flow. It is well known now that there is an absolute instability of the boundary layer which is linked to transition to turbulence, but convective routes are also observed. It is these convective modes that we focus on here. A comparison of three different approaches to investigate the convective, so called Type-I, stationary crossflow instability is presented here. The three approaches consist of local linear stability analysis, direct numerical simulations (DNS) and experiments. The ‘shooting method’ was used to compute the local linear stability whereas linear DNS was performed using a spectral-element method for a full annulus of the disk, a quarter and 1/32 of an annulus, each with one roughness element in the computational domain. These correspond to simulating one, four and 32 roughness elements on the full disk surface and in addition a case with randomly-distributed roughnesses was simulated on the full disk. Two different experimental configurations were used for the comparison: i) a clean-disk condition, i.e. unexcited boundary-layer flow; and ii) a rough-disk condition, where 32 roughness elements were placed on the disk surface to excite the Type-I stationary vortices. Comparisons between theory, DNS and experiments with respect to the structure of the stationary vortices are made. The results show excellent agreement between local linear stability analysis and both DNS and experiments for a fixed azimuthal wavenumber (32 roughnesses). This agreement clearly shows that the three approaches capture the same underlying physics of the setup, and lead to an accurate description of the flow. It also verifies the numerical simulations and shows the robustness of experimental measurements of the flow case. The effects of the azimuthal domain size in the DNS and superposition of multiple azimuthal wavenumbers in the DNS and experiments are discussed.

© 2015 Elsevier Masson SAS. All rights reserved.

1. Introduction

The rotating-disk flow has been of particular interest over the last century due to von Kármán's successful derivation of an exact similarity solution of the incompressible Navier–Stokes equations in cylindrical coordinates [1]. The flow belongs to a family of the so-called 'BEK boundary layers', including the Bödewadt, Ekman and von Kármán rotating boundary layers. These are characterized by a Rossby number (Ro), the definition of which is given in e.g.

Ref. [2]. For the von Kármán boundary layer the Rossby number is $Ro = -1$. Within the flow a thin three-dimensional boundary layer is generated by the rotation of the disk, and the laminar similarity solution is described by the three velocity components: U , V and W , in the radial, azimuthal and wall-normal directions, respectively, as depicted in Fig. 1. In this global picture, U and V increase linearly with radius (r) whereas W is constant in r , indicating that the boundary-layer thickness does not change as a function of the radial position. Using the viscous length scale $L^* = (\nu^*/\Omega^*)^{1/2}$, where ν^* is the kinematic viscosity, Ω^* the angular velocity and superscript * denotes a dimensional value, the Reynolds number is the nondimensional radius; $R = r = r^*/L^*$, where r^* is the dimensional local radius. In Fig. 1 it is also possible to see that the radial velocity profile includes an

* Corresponding authors.

E-mail addresses: ellinor@mech.kth.se (E. Appelquist), [\(P.H. Alfredsson\)](mailto:phal@mech.kth.se).

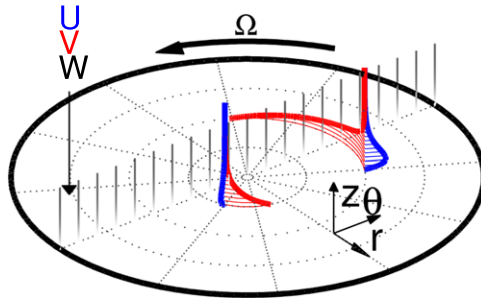


Fig. 1. The laminar velocity profiles of the similarity solution for the flow over a rotating disk. U is the radial velocity component, V is the azimuthal velocity component and the vertical greyscale lines indicate the amplitude of the wall-normal velocity component W (white denotes zero velocity). The cylindrical coordinates are given by r , θ and z , and the rotation rate is defined by Ω .

inflection point, which according to the Rayleigh stability criterion causes an inviscid instability. The existence of the exact similarity solution for the laminar flow led to a variety of possible approaches for analysing the flow further, creating a canonical model for other similar three-dimensional boundary layers, such as the flow over a swept wing. However, it is not only useful as a simple model of three-dimensional boundary layers but also to investigate its direct applications to rotating-flow configurations, such as turbomachinery, computer storage devices and chemical vapour deposition.

More than half a century ago experimentalists first found vortex structures in the rotating-disk boundary layer spiralling outwards with radius (e.g. Refs. [3–6]). These vortices are stationary within the rotating reference frame and correspond well to the convectively unstable stationary disturbances predicted by local linear stability analysis when using the viscous 6th-order perturbation equations (e.g. Refs. [7,8]). The vortices themselves are excited by small roughnesses on the disk surface, which are virtually unavoidable in experiments. Two different stationary modes exist that are unstable for certain parameter sets: the inviscid Type-I mode, so-called crossflow instability; and the viscous Type-II mode. The latter is attributed to the centrifugal and Coriolis forces, and has a higher critical Reynolds numbers than Type-I for stationary disturbances. Travelling Type-I and Type-II modes are also unstable over certain parameter ranges. Both stationary and travelling disturbances have been investigated by local linear stability analysis (e.g. Refs. [4,7,9–13]). Furthermore, there is a third mode, Type-III, which is a damped upstream-travelling mode that coalesces with the Type-I mode at higher Reynolds numbers. This coalescence results in the rotating-disk boundary-layer flow becoming locally absolutely unstable for some travelling disturbances above $R > 507$ [12,14]. Theoretical studies have been extended to take into account the flow development in the radial direction through global stability analysis. Pier [15] showed that the rotating-disk flow becomes nonlinearly globally unstable at the onset of local absolute instability.

This paper focuses on the Type-I crossflow stationary vortices and, even though there has been much research done both theoretically and experimentally in connection to these, only one set of direct numerical simulations (DNS) can be found in the literature. Davies and Carpenter [16] validated their linear velocity-vorticity discretization scheme by simulating Type-I and Type-II travelling waves excited by a radially-localized time-periodic wall displacement. A comparison with local theory with a stationary disturbance of azimuthal wavenumber 32 was also performed. They found that the locally-defined radial wavenumbers and growth rates from quasi-parallel linear stability theory were similar to the global linear DNS. This is also in accordance with the local-global investigation by Malik and Balakumar [17].

The purpose of this study is to compare local linear stability analysis with numerical simulations and experiments, and to establish how well they correspond to each other. In Section 2, technical descriptions of the theoretical, numerical and experimental methods are described. Linear simulations are presented to elucidate the global behaviour for disturbances triggered by regular and random distributed roughness elements, and results from two experiments will be presented, with and without deterministic surface roughness elements on the disk surface. In Section 3, the results from the comparison of the three approaches are given, which are then summarized in Section 4.

2. Description of the methods

2.1. Local linear theory

The description of the rotating-disk flow originates from the Navier-Stokes equations formulated in a cylindrical-coordinate system in the rotating frame of reference. The similarity equations for the mean flow, as formulated by von Kármán [1], were here solved numerically via a shooting method. Also, the perturbation equations that govern the linear local stability of the rotating-disk flow have been derived and solved. For the perturbation equations, the parallel-flow approximation is used to simplify the system of partial differential equations (PDE) to a sixth-order system of ordinary differential equations (ODE). This simplification means that spatial-development of the flow is neglected and only the local stability behaviour can be determined from this approach. It is possible to reduce the set of equations further by neglecting the Coriolis and streamline-curvature terms, which leads to the familiar Orr-Sommerfeld equation. However, in this context only the sixth-order system of ODE will be considered in line with the work of Lingwood [8], including rotation and curvature.

The ‘shooting method’ was used to investigate the local linear stability of this flow. This method includes a coordinate transformation before the normal-mode approximation is applied following the path of Lingwood [8]. For a stationary mode (in the rotating reference frame) considered here, the temporal frequency is zero ($\omega_r = 0$) and the disturbance is assumed to have the shape

$$\phi(r, \theta, z) = \psi(z) \exp[i(\alpha r + \beta \theta)] \quad (1)$$

for the disturbance vector $\phi = (u, v, w, p)^T$ and the amplitude vector $\psi = (\hat{u}, \hat{v}, \hat{w}, \hat{p})^T$, where the hat symbol denotes the spectral representation of the perturbation fields, and α and β are the radial and azimuthal wavenumber, respectively. The neutral stability curves for such a disturbance are shown in Fig. 2. The curves show the boundaries in terms of α_r , β and the angle

$$\varepsilon = \tan^{-1}(\bar{\beta}/\alpha_r), \quad (2)$$

where $\bar{\beta} = \beta/r$, along which $\alpha_i = 0$ (β is real by definition and $\omega_i = 0$ as a spatial analysis is performed). Within the curves α_i is negative and the disturbances are growing in the positive r -direction. Two branches are marked corresponding to the Type-I and II disturbances. For the local theory data shown in the result section of this paper, we have chosen to focus on the Type-I stationary vortices because they have higher spatial growth rates than Type-II. This difference is made clear in Fig. 3 where $-\alpha_i$ of Type-I, II and III stationary disturbances are plotted for $\beta = 32$.

The Type-III disturbance is an upstream mode, i.e. the group velocity is negative, that never becomes unstable for the stationary waves for these R and thus is not seen in the neutral curves in Fig. 2. Due to the difference in group velocity, the downstream modes, Type-I and II, are unstable for $\alpha_i < 0$ in contrast to Type-III for which instability occurs for $\alpha_i > 0$. The local theory data have also previously been compared with the results from parabolic stability equations (PSE), see [17,18], where the global PSE growth-rate data were found to be slightly higher than the local theory data for Type-I and II disturbances.

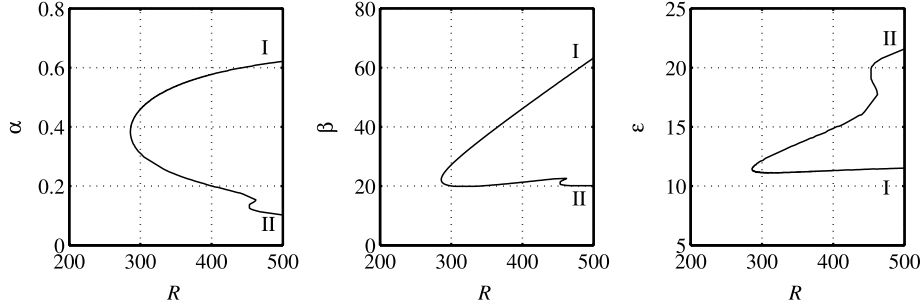


Fig. 2. Neutral curve ($\alpha_i = 0$) obtained from local linear spatial stability analysis for stationary disturbances ($\omega = 0$). Left to right; α_r , β and ε (in degrees). Two branches marked to correspond to the Type-I and II disturbances, due to the inviscid and viscous mechanism, respectively.

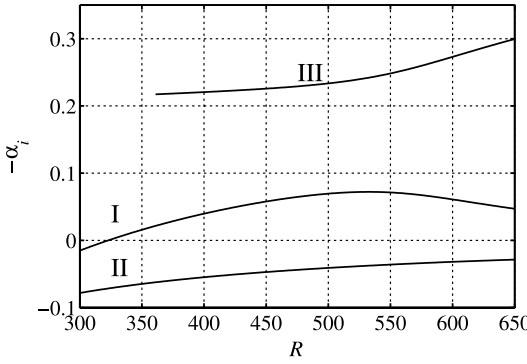


Fig. 3. Radial growth rate $-\alpha_i$ for stationary disturbances of Eq. (1) for $\beta = 32$. Type-I and II disturbances are denoted as in Fig. 2. The Type-III disturbance is an upstream branch, which emerges slightly above $R = 350$.

2.2. Direct numerical simulation (DNS)

The simulations were performed with the massively parallel spectral-element code Nek5000 [19]. Nek5000 solves the incompressible Navier–Stokes equations via a Legendre polynomial-based Spectral Element Method (SEM). SEM was introduced by Patera [20] and combines the geometrical flexibility of finite element methods with the accuracy of spectral methods. The orthogonal basis of Legendre polynomials up to degree N is used within each element, where $N = 7$ was chosen in our study to optimize both resolution and computation time. The solution to the Navier–Stokes equations is then approximated as an expansion of Lagrange interpolants. The pressure is expanded in polynomials of order N , as in the standard P_N – P_N method [21]. Between the various elements, C_0 continuity is maintained meaning that the values are continuous at the element borders whereas the derivatives may be discontinuous. The temporal discretization scheme BDF/EXT of second order is used [22] based on operator splitting, where the nonlinear convective terms are treated explicitly via an extrapolation scheme, and the viscous and divergence operators are treated implicitly [23].

Nek5000 is optimized for MPI-based (Message Passing Interface) usage on supercomputers [24], and the simulations in the present work were performed on 528, 1056 and 2112 cores.

2.2.1. Governing equations

The nonlinear terms can be turned off so that the code is run in only a linear fashion. This is the approach taken for our simulations presented here. For these linear simulations, the flow consists of a base flow and a perturbation on top of this flow. The von Kármán similarity solutions were used as base-flow components

Table 1

Spectral-mesh summary indicating size of the domain, number of spectral elements used and resolution in the radial, azimuthal and vertical directions. P refers to the part of the domain used, either 1, 4 or 32.

$r = [230 670]$	$N_r = 88$	$\Delta r = 5$
$\theta = [0 2\pi/P]$	$N_\theta = 11 \cdot 32/P$	$\Delta\theta = 2\pi/(11 \cdot 32)$
$z = [0 19.5]$	$N_z = 17$	$\Delta z = 0.3, s = 1.15$

($\mathbf{U} = (U, V, W)$). The Navier–Stokes perturbation equations, which Nek5000 solves, are

$$\frac{\partial \mathbf{u}_x}{\partial t} + \mathbf{u}_x \cdot \nabla \mathbf{u}_x + \mathbf{u}_x \cdot \nabla \mathbf{U}_x = -\nabla p + \frac{1}{R} \nabla^2 \mathbf{u}_x + \mathbf{f}_x \quad (3)$$

together with the continuity equation

$$\nabla \cdot \mathbf{u}_x = 0, \quad (4)$$

where $\mathbf{u}_x = (u_x, u_y, w)$ are the perturbation velocities in Cartesian coordinates, p is the pressure and \mathbf{f}_x is a forcing term used in connection with the initial disturbance and sponge regions. The von Kármán base flow is translated to Cartesian coordinates ($\mathbf{U} \rightarrow \mathbf{U}_x$) before entering Nek5000, and when the simulations are finished, the perturbation velocities are translated to cylindrical coordinates for further analysis ($\mathbf{u}_x \rightarrow \mathbf{u}$).

For the case of the rotating-disk flow, the reference velocity, pressure and time scales used in the non-dimensionalization are $r^* \Omega^*$, $\rho^* r^{*2} \Omega^{*2}$ and $L^*/(\Omega^* r^*)$, respectively. Here, ρ^* is the dimensional density. The time scale within Nek5000 is then such that t corresponds to the number of radians through which the disk has rotated. $T = t/(2\pi)$ is used as the number of full rotations of the disk.

2.2.2. Mesh

The resolution of the spectral-element mesh used for all simulations is shown in Table 1 and in Fig. 4 for 1/32 of the annulus. The polynomial expansion was made within each of these elements. While the simulations are described as sections of an annulus, the solver itself is based on Cartesian coordinates. The angular extent of the domain is $2\pi/P$, where P is either 1, 4 or 32, limiting the simulations to certain azimuthal wavenumbers. The ratio $r \Delta\theta / \Delta r$ of an element was 0.82 at the inner part of the mesh and increased outwards with a maximum ratio of 2.4. In the wall-normal (z) direction the elements were stretched according to

$$z_n = \sum_{i=1}^n z_1 s^{i-1}, \quad (5)$$

where s is the stretch factor, z_n is the coordinate at position n above the wall ($z_1 = \Delta z$ where Δz is the extent of the spectral element

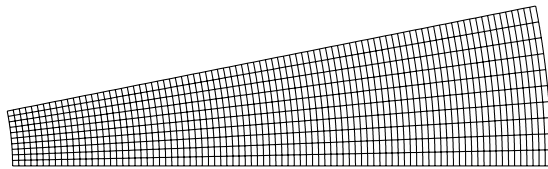


Fig. 4. The spectral-element mesh used for run DNS_R32. This mesh contains 11 elements in the θ -direction and 88 elements in the r -direction, further information is given in Table 1.

closest to the wall). An advantage of defining the coordinate system in such a way is the equivalence to the geometric sum

$$z_n = \frac{s^n - 1}{s - 1} \Delta z. \quad (6)$$

For our simulations, $\Delta z = 0.3$ with 17 elements taken to a height of $z = 19.5$ with $s = 1.15$. All the simulations were simulated in the (non-rotating) laboratory frame of reference. The Courant–Friedrichs–Lowy (CFL) condition was 0.15.

2.2.3. Boundary conditions

The boundary conditions for the linear simulations were the same as in Ref. [25] and are briefly described below. A sponge region was used just ahead of the outer radial boundary that forces the flow back to the von Kármán similarity solution and, therefore, smoothly damps out all the flow perturbations. In our simulations, the sponge function was adapted from [26]. The flow velocities at the disk were specified as no-slip and non-penetration conditions, and for the top boundary condition the following combination of Dirichlet and stress-free conditions was used: the perturbation velocities in the wall-parallel directions were set to zero ($u_x = 0$ and $u_y = 0$), whereas the wall-normal velocity (w) was set to follow the stress-free Neumann boundary condition for the corresponding weak formulation, here resulting in $dw/dz = p$, normalizing the pressure of the simulation by the vertical gradient of the inflow. The segmentation of the domain from the full rotating annulus to only $2\pi/P$ radians was made possible through cyclic boundary conditions in the azimuthal direction, which are essentially periodic boundary conditions but involve an appropriate rotation of the velocities across the boundary.

2.2.4. Roughness

The influence of distributed surface roughness was modelled by a continuous volume force applied in the near-wall region of the rotating disk. To excite the flow continuously, a Gaussian forcing function was used

$$\eta = \exp\{-\lambda[(x - x_{ex})^2 + (y - y_{ex})^2] - \mu(z - z_{ex})^2\}, \quad (7)$$

where x, y and z are the spatial locations where the function is evaluated and x_{ex}, y_{ex} and z_{ex} are the spatial locations of the excitation. The forcing function is stationary with respect to the disk. In the rotating reference frame, therefore, the forcing function is stationary but in the laboratory frame for our simulations it is moving in the azimuthal direction with the disk speed. The parameters λ and μ define the constant z -plane extent of the roughness and the vertical height of the roughness, respectively. The four simulations performed can be seen in Table 2 and are described further in the next Section 2.2.5. However, the chosen radial position for the disturbance for DNS_R01, DNS_R04 and DNS_R32 was $r_{ex} = 270$, and is connected to the Cartesian coordinates in the laboratory frame via $x_{ex} = r_{ex} \cos(\Omega t)$ and $y_{ex} = r_{ex} \sin(\Omega t)$. Since the disturbance should act as a roughness, it was placed on the disk surface, i.e. $z_{ex} = 0$. The number of disturbances for DNS_R01r was 21, and r, λ and μ were generated through a

Table 2

The various DNS runs where the number of simulated roughnesses refers to a full disk, the degrees denote the angular extent of the domain and T is the number of full time periods (of revolution of the disk) included in the simulation. All simulations were performed in the laboratory frame of reference except for the last quarter revolution, $T = 3 - 3.25$, of DNS_R01r, which was performed in the rotating frame of reference.

Name	T [rotations]	$^\circ$ [degrees]	# roughnesses
DNS_R01r	3.25	360	21
DNS_R01	6	360	1
DNS_R04	6	90	4
DNS_R32	6	11.25	32

script. The limitations for randomly generating these values were: $250 \leq r \leq 350$; $1.38 \cdot 10^{-2} \leq \lambda \leq 12.5 \cdot 10^{-2}$; and $0.5 \leq \mu \leq 50$. For the other simulations, $\lambda = 1/(2 \cdot 3^2) = 5.56 \cdot 10^{-2}$ and $\mu = 1/(2 \cdot 0.2^2) = 12.5$.

Eq. (7) entered the simulations through the equation

$$\mathbf{f} = \eta(\mathbf{U}_d - \mathbf{U}_s), \quad (8)$$

where $\mathbf{U}_d = (0, 1, 0)$ is the velocity of the disk and \mathbf{U}_s is the current simulation velocity corresponding to the von Kármán laminar solution at all times. A translation of \mathbf{f} to \mathbf{f}_x allowed inclusion in Eq. (3).

2.2.5. Simulations

Four simulations have been performed, which differ in the azimuthal extent of the domain. The simulations are summarized in Table 2, where part of the name indicates the size of the domain, i.e. a full annulus (01), a quarter of an annulus (04) or 1/32 of an annulus (32). Each simulation except DNS_R01r has one roughness element within the domain, giving rise to different results due to the different azimuthal wavenumbers permissible within the given domain size. The simulation DNS_R01r has randomly distributed roughnesses in the domain within limits that are described in Section 2.2.4.

The computations have been carried out for long enough times to obtain a converged state for the energy amplitude. The kinetic energy of the fluctuations at a specific radial position is here defined as

$$E(r) = \int_{\theta_1}^{\theta_2} \int_0^Z \frac{1}{2} \left[\left(\frac{u}{r} \right)^2 + \left(\frac{v}{r} \right)^2 + \left(\frac{w}{r} \right)^2 \right] dz d\theta, \quad (9)$$

where u, v and w represent the cylindrical velocity perturbations obtained from the DNS and Z is the total wall-normal height of the domain. The perturbation velocities are thus normalized by the local radius before the energy is calculated, corresponding to an energy calculation at $r = 1$. The reason for this normalization is to calculate a measure that is comparable with local theory where, unlike the global case, there is no underlying linear radial increase. In calculating the convergence of \sqrt{E} (which has the same order as the normalized velocities) for all simulations, the square root of the integral value from Eq. (9), where $\theta_1 = t$ and $\theta_2 = 2\pi/32 + t$, is shown in Fig. 5(a). Since only a section of azimuthal extent $2\pi/32$ is considered at one time the level of the curves is arbitrary. The lower values of DNS_R01 are explained by the fact that the stationary field rotating with the disk included in Eq. (9) is just in front of the roughness. The data obtained at other radial positions qualitatively show the same picture, and are therefore not shown here. All simulations become stationary in time within three rotations except DNS_R01r. For this simulation, at times larger than $T = 3$, the grid resolution was elevated from polynomial order $N = 7$ to $N = 9$ to check whether the instationary behaviour was due to a lack of resolution, although no change occurred. The curve in Fig. 5(a) does, however, show a repeated pattern each rotation from approximately $T = 1$ to $T = 3$, and when changing the reference

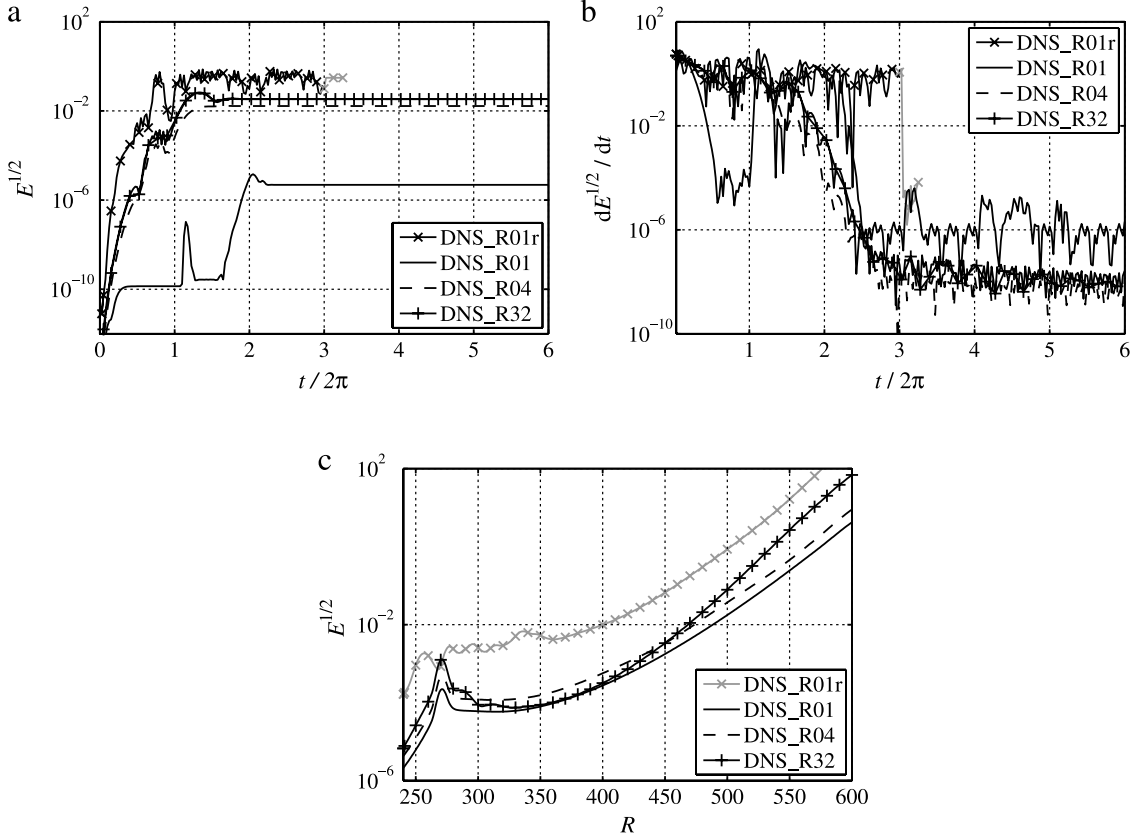


Fig. 5. (a) Energy $\sqrt{E(r=500)}$ as a function of time is shown for all runs. (b) The derivative in time of $\sqrt{E(r=500)}$. (c) The resulting energy profile $\sqrt{E(r)}$ at the last timestep.

frame by adding the Coriolis term as a forcing, \mathbf{f}_x in Eq. (3), it became stationary in time. The derivative in time of the curves in Fig. 5(a) are plotted in Fig. 5(b), showing that DNS_R01r converges to the same level as DNS_R01 for later times than $T = 3$. This level corresponds to the tolerances set in Nek5000. The reason for the instationary behaviour at earlier times is therefore shown to be due to the roughnesses added as forcings passing through the (non-equidistant) grid in the laboratory frame of reference. The spatial extent of the roughnesses in this simulation was smaller than for the other cases, e.g. DNS_R01, where stationary behaviour was observed, and increased resolution was insufficient to resolve the difference. When DNS_R01r showed a consistent behaviour to the other simulations the simulation was stopped, and for further analysis, the last field analysed is at $T = 3.25$.

In Fig. 5(c), the resulting energy profiles at the last timestep of the simulations are shown where $\theta_1 = 0$ and $\theta_2 = 2\pi$ in Eq. (9). The excitation of the flow by the numerical roughness at $r_{ex} = 270$ creates a locally-elevated amplitude and, due to the different wavenumbers within the domain (multiples of 1, 4 and 32 being permitted in the respective cases), the amplification with R is slightly different between the runs.

2.3. Experiments

The details of the experimental setup are described in Refs. [6,27,28] and the setup is shown in Fig. 1 in [27]. A well-polished glass disk with a radius of $r_d^* = 235.5$ mm is mounted on an aluminium-alloy disk, which is connected to a vertical shaft of a d.c. servo motor. The main shaft is sustained by an air bearing so that low disturbance levels are ensured during the operation. The velocity measurements were performed by constant temperature

Table 3

Experimental conditions. Here, the R_{edge} is Reynolds number based on the disk radius, r^* is the local radius of the hot-wire probe, Ω^* the rotational speed, N_R is the number of roughness elements and z the normalized wall-normal position.

Case	R	R_{edge}	r^* [mm]	Ω^* [rpm]	N_R	z
EXP_clean	360–605	618	137–231	1000	–	1.3
EXP_rough	260–605	615	100–232	1013	32	1.3

anemometry (CTA) using a single hot-wire probe. The hot-wire probe was mounted on a traverse system and the sensor aligned with the radial direction so that it was sensitive mainly to the azimuthal velocity component. The traverse system consists of two axes: one in the radial direction and the other is mounted on the radial traverse at a 45° angle so not to disturb incoming flow over the hot-wire probe. Voltage outputs from the CTA were sampled by a 16 bit A/D converter with a sampling rate of 720 samples/rotation and the sampling time was 60 s for each measurement position.

Experiments with two surface conditions were performed in the present study. One called the 'clean-disk' condition, i.e. without any artificial surface roughness elements added to the well-polished disk surface. However, even when using the clean disk, Type-I stationary vortices are excited by unavoidable surface roughnesses on the surface. It was expected that the multiple unstable azimuthal wavenumbers of the Type-I stationary vortices would be naturally selected in the unstable region, following the neutral curve for convective instability of the rotating-disk boundary-layer flow. The second case had 32 artificial surface roughness elements placed on the disk surface. Each roughness element was created using dry transfer lettering supplied by Letraset® (Letraset Ref. 13045). Each roughness had a circular shape and the diameter was approximately 2 mm with an average height of about $5.4 \mu\text{m}$. They were put on the disk at approximately

$r^* = 110$ mm, corresponding to $R = 287$, and equally spaced in the azimuthal direction. The 32 roughness elements continuously excite stationary disturbances with $\beta = 32$ and that mode is shown to become dominant in the flow field. This simplifies the comparison with local linear stability analysis and DNS with a fixed wavenumber of 32. Herein, this case is referred to as the 'rough-disk' condition.

Table 3 shows experimental conditions used in this study where EXP_clean and EXP_rough, correspond to clean- and rough-disk conditions, respectively. The azimuthal velocity at a constant wall-normal height, $z = 1.3$, was measured with a step of $\Delta R = 5$. To maximize the signal-to-noise ratio, for EXP_clean case, the signals were filtered with a band-pass filter $17 < \omega^*/\Omega^* < 70$ below $R \leq 490$ and with a high-pass filter $17 < \omega^*/\Omega^*$ for $495 \leq R \leq 525$ and, for EXP_rough case, a band-pass filter $17 < \omega^*/\Omega^* < 70$ below $R \leq 415$ and a high-pass filter $17 < \omega^*/\Omega^*$ for $420 \leq R \leq 450$ were applied. Azimuthal mean velocity profiles at low Reynolds numbers in these two cases were also performed and were found to be in good agreement with the theoretical laminar profile.

3. Results

The comparisons made within this section are between the local linear theory, the DNS (see Table 2) and the experiments (see Table 3). In Fig. 6 the data from all the simulations and experiments performed are shown as r - θ fields at a nondimensional height of $z = 1.3$. For Fig. 6(a)–(d) the perturbation velocity fields $\log_{10} |v/r|$ at the last timestep of the four linear simulations: (a) DNS_R01, (b) DNS_R04, (c) DNS_R01r and (d) DNS_R32 are shown. The radial extent of the domain shown is $r = 240$ – 600 , i.e. without sponge regions. Each of the simulations (a), (b) and (d) contains one roughness element, which generates stationary vortices. For DNS_R01, even at the largest radius, the vortices are not covering the entire disk, and for DNS_R32 there is only one vortex seen for all radial positions, i.e. 32 for the full disk. In (c), the randomly distributed roughnesses are shown on the disk. In Fig. 6(e) and (f), contour maps of ensemble-averaged azimuthal velocity time series where the mean is subtracted from the experimental data are shown, also here in logarithmic scale. The azimuthal velocity is normalized with the azimuthal speed of the disk at each radial location for correspondence to the local scale in the experiments. For the clean-disk case seen in Fig. 6(e), EXP_clean, stationary vortices are shown due to excitation by unavoidable surface roughnesses and this case is comparable to the randomly-distributed roughnesses of DNS_R01r in Fig. 6(c). For the rough-disk experiment seen in Fig. 6(f), EXP_rough, 32 stationary vortices are clearly shown arising from the roughnesses and, for larger radial positions, breakdown of the stationary vortices (being a nonlinear process this is avoided by the linear DNS). The setup of this experiment is comparable to DNS_R32. Both experiments contain nonlinearities at large Reynolds numbers. The onset of nonlinearity in these experimental studies is defined to be where the amplitudes of the harmonics reach a threshold of 10^{-6} in the power-spectrum scale, which is the same as used in Ref. [28]. For EXP_clean this is above $R = 510$ and for EXP_rough this is above $R = 415$.

3.1. Comparison of linear region with 32 vortices

In this section, only EXP_rough and DNS_R32 are compared to linear theory since the wavenumber $\beta = 32$ is excited in both these cases simplifying the comparison. From local theory, the eigenfunctions of each velocity component were calculated for $R =$

375 and $\beta = 32$ of the Type-I mode ($\omega = 0$ and $\alpha = 0.44 - i0.024$) and were compared with the DNS quantities from DNS_R32

$$u_{\text{rms},\text{DNS}}^2 = \int_0^{2\pi} \frac{1}{2} \left(\frac{u}{r} \right)^2 d\theta, \quad (10a)$$

$$v_{\text{rms},\text{DNS}}^2 = \int_0^{2\pi} \frac{1}{2} \left(\frac{v}{r} \right)^2 d\theta, \quad (10b)$$

$$w_{\text{rms},\text{DNS}}^2 = \int_0^{2\pi} \frac{1}{2} \left(\frac{w}{r} \right)^2 d\theta. \quad (10c)$$

The experimental stationary disturbance amplitude, $v_{\text{rms},\text{EXP}}$, is defined as the root mean square of ensemble-averaged azimuthal fluctuation velocity time series with 32 roughness elements.

The comparison in Fig. 7 shows that the amplitude functions for simulations, experiments and theory all correspond extremely well. At this R , the velocity peak of v_{rms} is located at $z = 1.5$ but it moves towards the wall as R increases (not shown).

As already stated, only Type-I stationary vortices are considered here, and in Fig. 8 data from DNS and experiments are shown where the data have been obtained by tracing the peaks of the 32 vortices around the disk (for DNS_R32 and EXP_rough). From the traced vortices, further information about the angles and growth rates was calculated. In the DNS, denoting the amplitude of the azimuthal velocity perturbation normalized by the radial position as $\Delta v_{0.5}$, the growth rate for each vortex, $d[\ln(\Delta v_{0.5})]/dr$, was obtained calculating the linear slope of the logarithmic $\Delta v_{0.5}$ values by using the least-mean-square method spanning over $\Delta R = 20$. In the same way, the growth rate of the experimental vortices was obtained using ensemble-averaged azimuthal velocity fluctuation time series from EXP_rough, which were also normalized by the local speed of the disk in order to be comparable to local theory. This growth rate can then be compared with $-\alpha_i$ in Eq. (1) obtained from theory. The angle of each vortex in degrees, ε , between the azimuthal and the vortex direction was calculated following equation (1) in Ref. [5]

$$\tan \varepsilon = \frac{1}{r} \frac{dr}{d\theta} \Big|_s = \frac{\bar{\beta}}{\alpha_r}, \quad (11)$$

where $s(r, \theta)$ is the radial locus of the vortex and again $\bar{\beta} = \beta/r$. To derive the angle from the DNS, a span of $\Delta R = 5$ was used, and to smoothen the data a running average over $\Delta R = 20$ was taken. Having derived ε from the DNS data, α_r can be calculated from Eq. (11), assuming $\beta = 32$. The angle ε and α_r of stationary vortices from the experimental data were calculated using a range of $\Delta R = 30$ for each.

In Fig. 8, the DNS and experimental data are compared to local linear theory, which is included in the same figure. In Fig. 8(a), growth-rate data of the single vortex from DNS_R32 are shown and the growth rates from EXP_rough are denoted with blue markers (Δ), both following the theoretical growth rate curve ($-\alpha_i$) for $\beta = 32$. The theoretical data are shown in black for each integer β from 20 to 32, where 24, 28 and 32 are solid lines. The experimental data are only included for the linear region. In Fig. 8(b), the angle ε is shown on the ordinate from DNS_R32, EXP_rough and local theory, with β isolines. Also, the neutral curve from local theory is included as a thick black line. The vortex data for ε are seen to follow the curve of $\beta = 32$ closely, implying that α_r also agrees with theoretical data (see Eq. (11)). This is also shown in Fig. 8(c) where the growth rate (α_i) is plotted as a function of α_r , where again the experimental and simulation data follow the theoretical line of $\beta = 32$. From Fig. 8 it can be concluded that when a homogeneous field of 32 vortices is produced either in experiments or in simulations, the local theory predicts the global behaviour well.

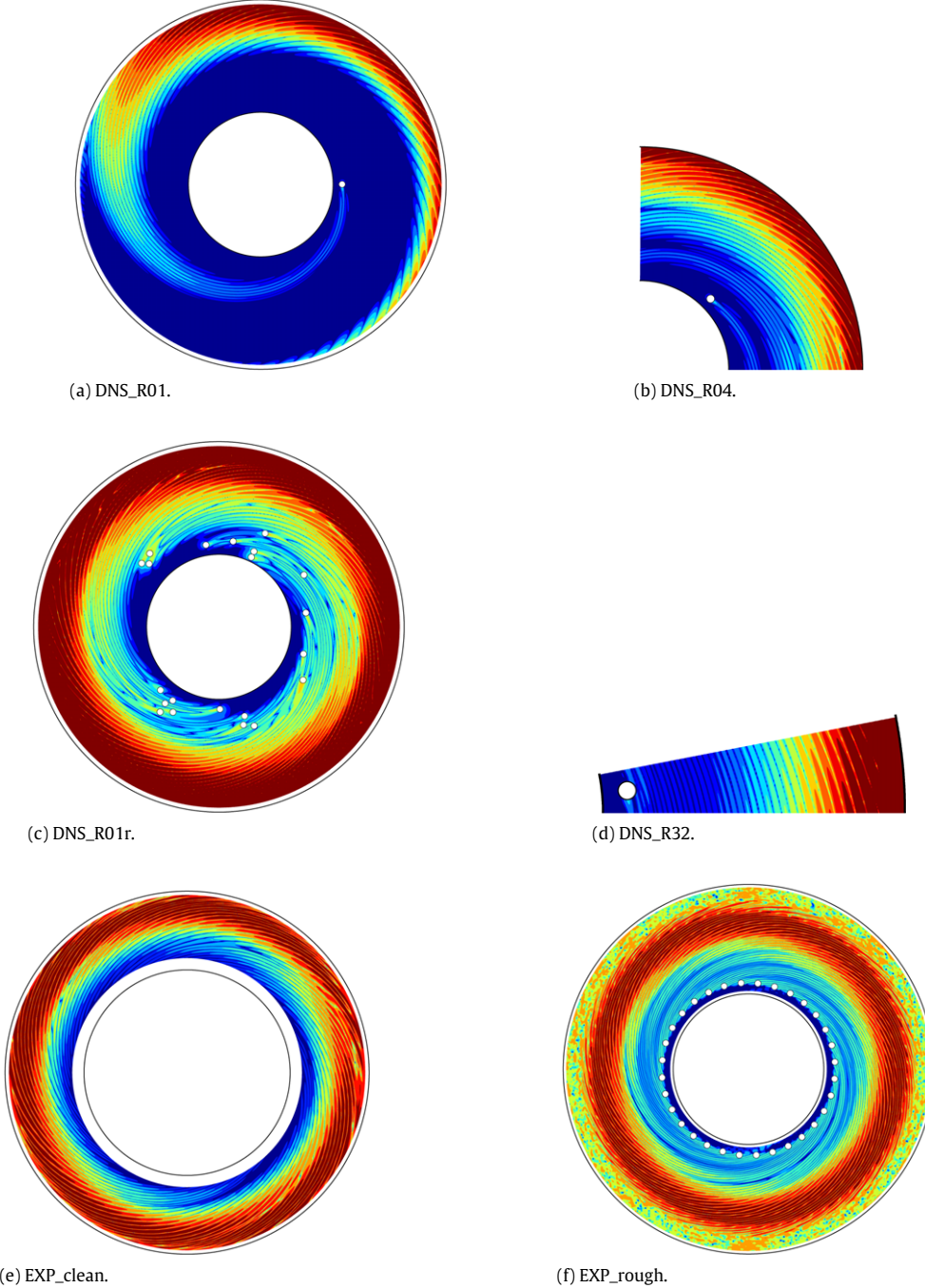


Fig. 6. (a)–(d) DNS fields of $\log_{10} |v/r|$ at $z = 1.3$ for the last frame of each simulation showing $R = 240 - 600$. The colour-scale range includes a 4.5 span. (e) and (f) The experimental fields measured at $z = 1.3$ and the colour bar denotes $-5 < \log_{10} |v/r| < -1.5$, which is a smaller range than for the DNS since the stationary disturbance amplitudes are saturated at large R due to nonlinear effects. In (a), (c), (e) and (f) the outer black line is at position $R = 615$ and all figures showing the full disk are thus comparable in size. However, the depicted size of the roughness is not to scale.

The growth rates for $\beta = 32$ from DNS_R01 and DNS_R04 were extracted via Fourier transforms and also plotted in Fig. 8(a) however all the simulation data fell on top of each other, as expected, and very close to the vortex data from DNS_R32 (not shown).

3.2. Comparison of linear region with varying number of vortices

Instead of forcing the wavenumber to $\beta = 32$, the simulations DNS_R01, DNS_R04 and DNS_R01r, and the experiment EXP_clean let the flow select the number of vortices as a function of radial position albeit DNS_R04 restricted the number of vortices to be

a multiple of four. The most straightforward analysis for a field of stationary vortices is simply to count the vortices around the disk. The outcome of that analysis is shown in Fig. 9(a) from simulations and experiments. For both DNS_R32 and EXP_rough, as expected, 32 vortices are clearly seen for all R . Experimental and DNS data have the best correspondence for DNS_R01r, DNS_R04 and EXP_clean since the vortices fill the disk area while they are still allowed to change with R (as a multiple of four for DNS_R04) due to the less restricted azimuthal domain. For DNS_R01, the vortices do not cover the entire disk and therefore a lower number is obtained (a cutoff threshold for the peaks of five orders smaller than the largest amplitude at the specific radial location was used).

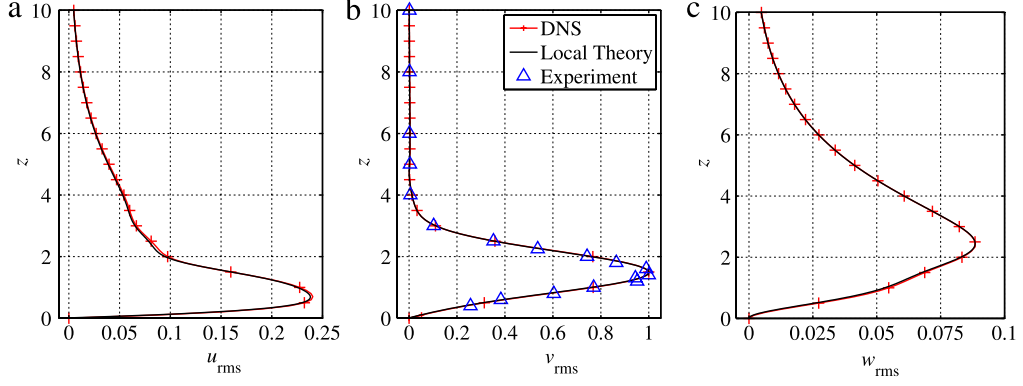


Fig. 7. Eigenfunctions at $R = 375$ for $\beta = 32$ normalized by the maximum value of v_{rms} . From left to right: u_{rms} , v_{rms} and w_{rms} where the DNS data corresponds to $u_{\text{rms},\text{DNS}}$ from Eq. (10) and the experimental data corresponds to $v_{\text{rms},\text{EXP}}$ normalized by the maximum value from EXP_rough. The local theory data have a fixed $\omega = 0$ and $\alpha = 0.44 - i0.024$.

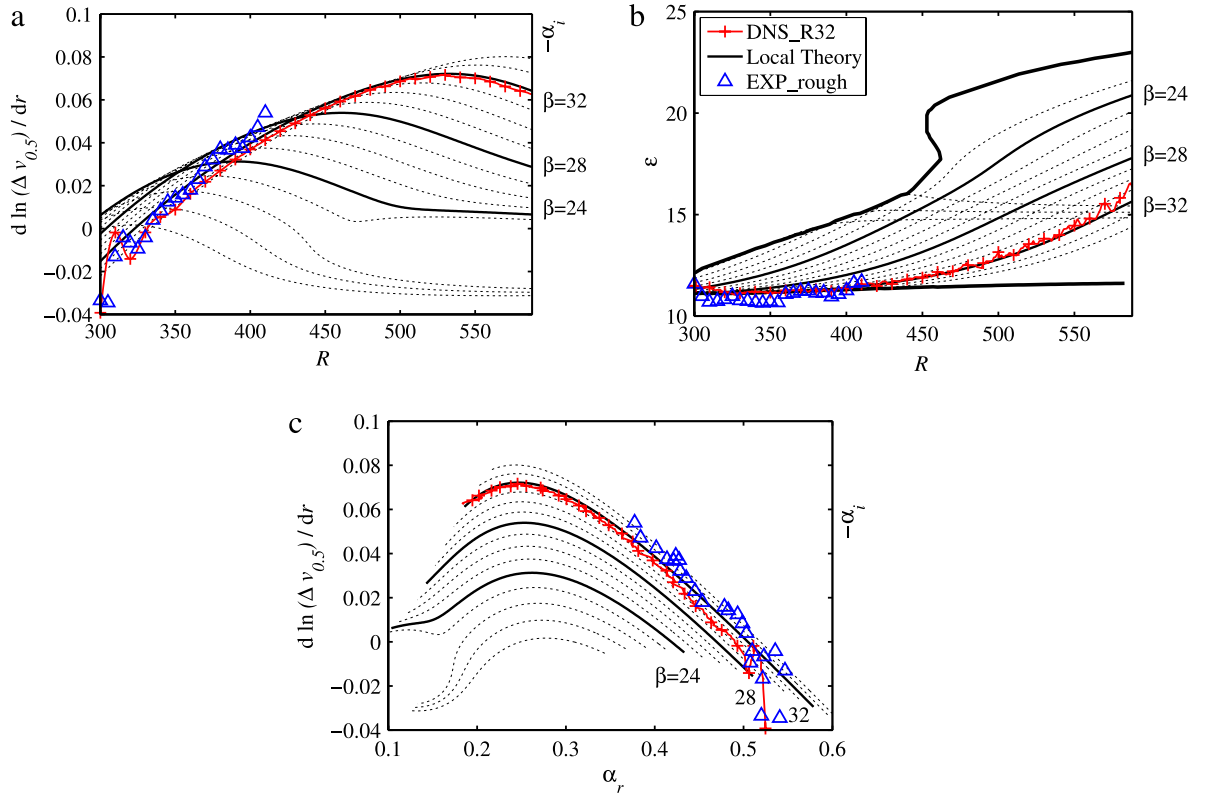


Fig. 8. Comparison between local theory ($\omega = 0$), DNS_R32 and EXP_rough, experiments and DNS, where the key is seen in (b). (a) The growth rate obtained by tracing the vortex peaks in the DNS and experiments. (b) The angle of the vortex in degrees. (c) The growth rate as a function of radial wavenumber. In all figures, theoretical data of $-\alpha_i$ are included for isolines of integer values $\beta = 20 - 32$. Solid lines correspond to $\beta = 24, 28$ and 32 . In (b) also the neutral curve for ε is included (thick solid lines).

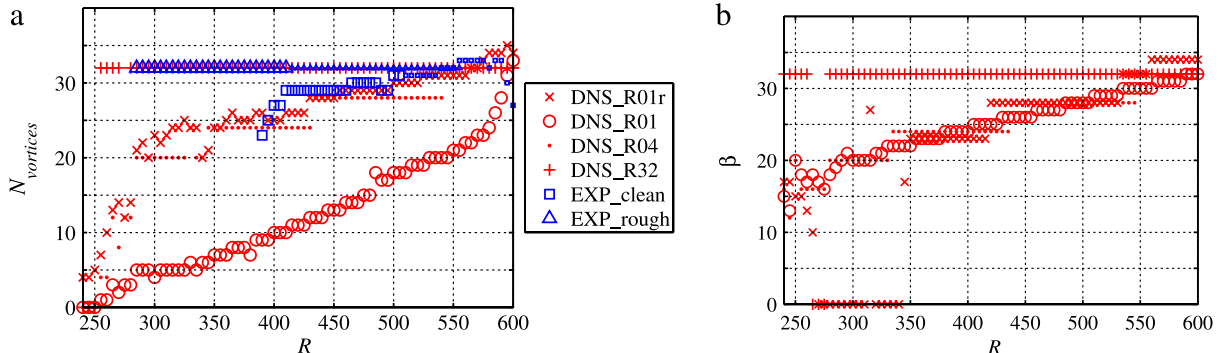


Fig. 9. (a) The number of vortices around the disk as a function of R given by counting the peaks of the azimuthal velocity field at a height of $z = 1.3$. The smaller symbols from the experimental data indicate a nonlinear regime. (b) The strongest wavenumber β from the spectra of the signal used in (a) for DNS only.

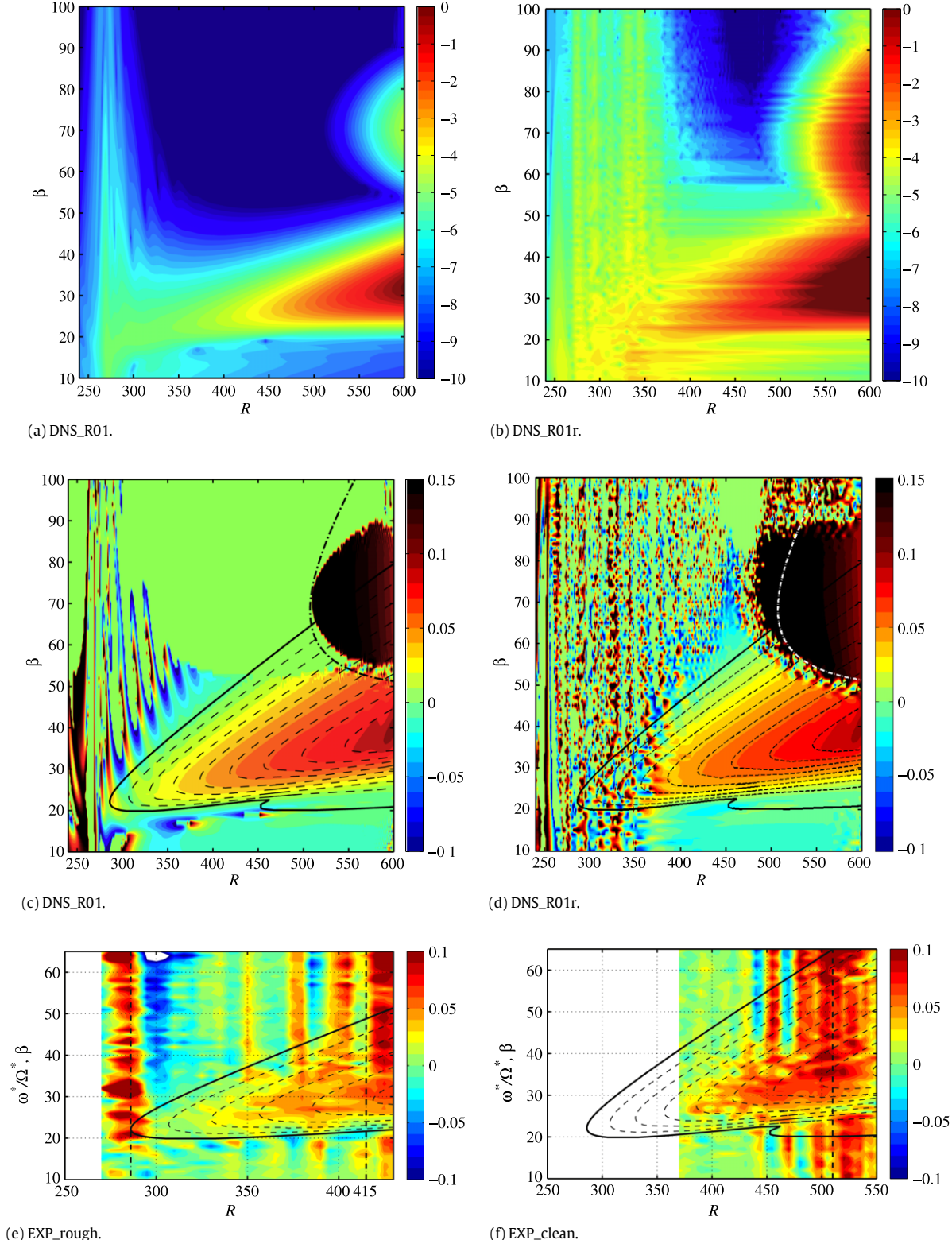


Fig. 10. (a)–(b) Contour plot of the power spectra in \log_{10} scale for the last timestep of v/r from DNS_R01 and DNS_R01r. (c)–(d) Contour plot of the growth rate in R from the data in (a)–(b). (e)–(f) Contour plot of the growth rate calculated from the power spectra from v of EXP_rough and EXP_clean, respectively. (c)–(f) Local theory data for stationary disturbances ($\omega = 0$) are shown where the solid line is $\alpha_i = 0$, with dashed lines showing positive spatial growth rate in steps of $\Delta\alpha_i = -0.01$, corresponding to the step change in colour from the contours. The chain line in (c) and (d) (for which $\omega \neq 0$) corresponds to the curve for neutral absolute instability ($\partial\omega/\partial\alpha = 0$).

For large R , the experimental data show nonlinear behaviour (small symbols) and for EXP_clean one sees a decrease in the number of vortices. Fig. 9(b) shows the strongest azimuthal wavenumber β extracted from DNS via Fourier transforms. The markers of DNS_R01 now correspond well to the other simulations since β is

related to the distance between the waves seen in Fig. 6(a). Note that for DNS_R01r the roughnesses are placed up to $r = 350$.

Presenting the spectral data from the simulation as a function of β and R , contour plots of the power spectra in \log_{10} scale are shown in Fig. 10(a)–(b) for the last timestep from the normalized

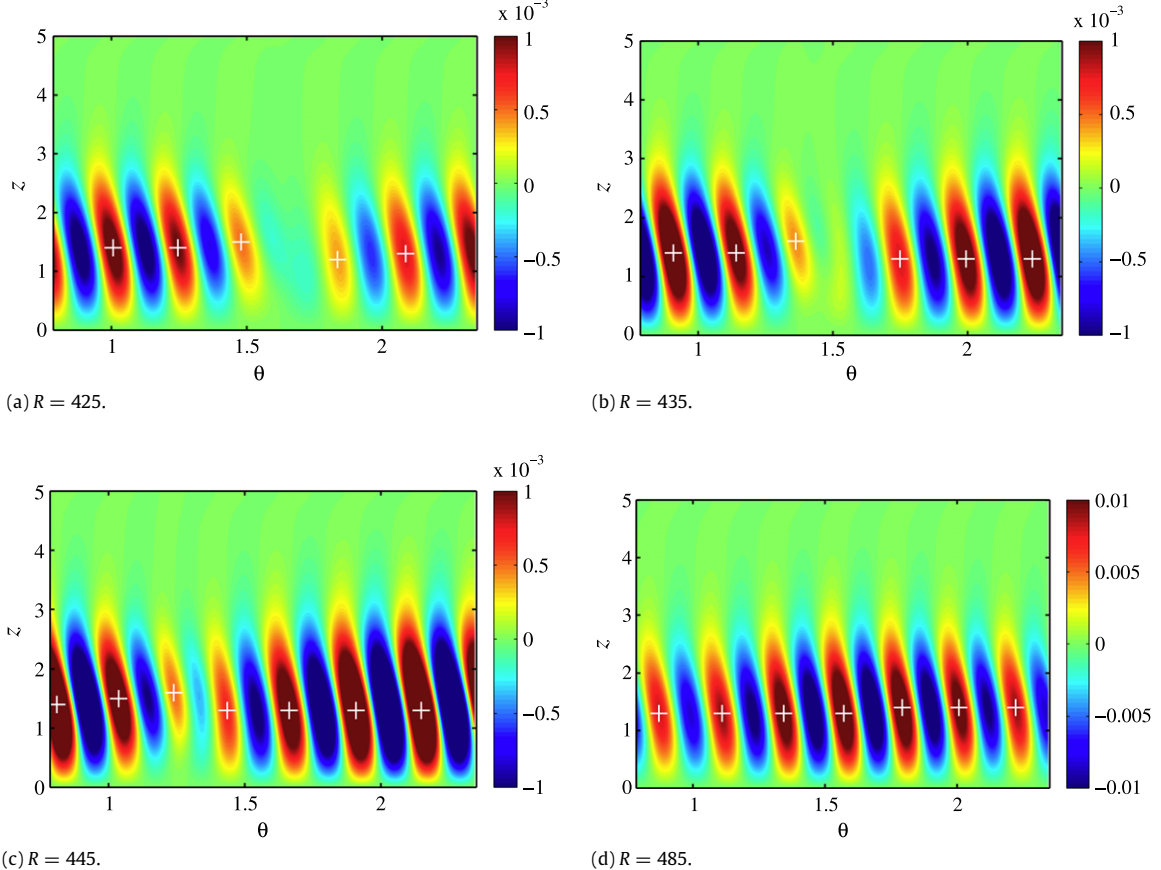


Fig. 11. Contour field in the $z\text{-}\theta$ plane of v/r for DNS_R04 at various radial positions showing a new vortex entering the flow field, (a)–(c), and a field of vortices of approximately same amplitude, (d). White crosses indicate maxima positions.

azimuthal velocity field, v/r , of DNS_R01 and DNS_R01r, and the growth rate in R is shown in (c)–(d) with theoretical growth-rate curves included. All data in Fig. 10 is taken at a height of $z = 1.3$. In figure (a) it is clear that there is a wide frequency band introduced by the roughness at $R = r = 270$, which dampens out for higher R where the strongest amplitude for each R is shown in Fig. 9(b). For (b) this is not as clear since there are many roughnesses occupying the area from $R = 250\text{--}350$. For both simulations in (a) and (b), there is a weak second peak present above $R \approx 500$ with an amplitude slightly decaying in time (not shown). This peak corresponds to the upstream mode produced by the absolute instability close to the end of the domain described in Ref. [25]. In (c)–(d) this second peak is found to have a high growth rate in space occupying the dark upper colour scale, lying inside the unstable area of the neutral curve for absolute instability. The data with lower amplitudes than 10^{-10} were filtered out in (a)–(b) to produce the growth rate figure in (c)–(d). It is clear from these figures that there is almost a perfect match between linear DNS and local theory data. When taking the Fourier transform of the DNS data the normalized azimuthal velocity field, v/r , at the last timestep is used. For the experiments the measured signal creating the power spectra was in time, and the data was ensemble averaged before calculating the growth rates to extract only the stationary modes for presentation in figures (e)–(f), showing growth rates of EXP_rough and EXP_clean, respectively. More on the experimental spectra can be found in Ref. [6]. Also the experimental data (e)–(f) are shown to have a correspondence to local theory. The absolute-unstable regions within the unstable area of the neutral curves shown in (c)–(d) are the only places where travelling ($\omega \neq 0$) unstable modes are considered within this paper. In order to focus solely on the stationary modes, the DNS have purely stationary-mode excitation; the experimental data are ensemble averaged,

which averages away any travelling and unsteady disturbances. Ibayama et al. [28] gives more detailed analysis of experiments with clean disks where it is also clear that the travelling modes have much lower amplitude than the stationary modes.

Based on the initial amplitudes of the various wavenumbers created by the roughnesses at small R , the waves grow and decay according to their growth rates (α_i) in R . The many wavenumbers present in experiments and simulations create patterns of superposed waves and when following the highest amplitude wavenumber in R the initial amplitudes thus matter. When the roughnesses introduce small amplitudes of all wavenumbers, a continuously increasing discrete spectrum of β can be followed, see e.g. DNS_R01r in Fig. 9(a). If instead one of the wavenumbers is preferentially excited initially, this wavenumber will dominate the observed pattern. If this is $\beta = 32$ it will dominate at all radial positions due to its large growth rates as seen for EXP_rough however the growth rates themselves will, of course, still follow local theory, see Fig. 10(e). A single roughness excites all possible wavenumbers approximately equally (depending on the domain size in DNS), and as the highest growth rate moves to a higher β with increasing R , new vortices appear at larger R . Figs. 11 and 12 plot the azimuthal velocity, v/r , at various radial positions for DNS_R04, DNS_R01 and DNS_R01r in the $z\text{-}\theta$ plane. Fig. 11(a)–(c) highlights how a new vortex enters the flow field in DNS_R04 when β shifts from 24 to 28, and (d) shows an example where all vortices have approximately equal amplitude. With increasing radius, at some point the existing array of vortices breaks up, and a dislocation is created. This gap in turn, once grown sufficiently large, then accommodates a new vortex, as shown in the plot sequence. Fig. 12(a), on the other hand, presents the wavepacket of DNS_R01 localized at small θ . In (b), DNS_R01r is shown for the

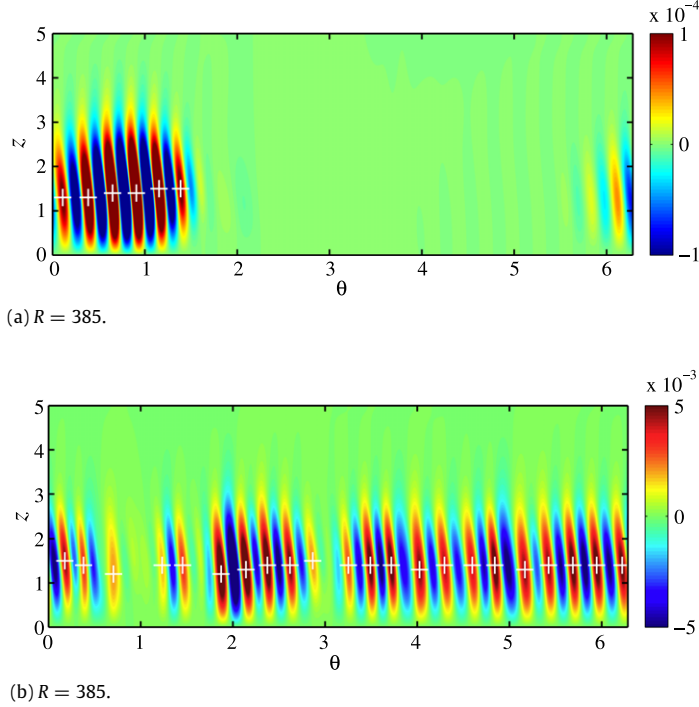


Fig. 12. Contour field in the z - θ plane of v/r for (a) DNS_R01 and (b) DNS_R01r. White crosses indicate maxima positions.

same radial position but where vortices of various amplitudes are present across all θ . Similar dynamics are exhibited by EXP_clean where unavoidable roughness elements are present at various positions on the disk surface. The white crosses in Figs. 11 and 12 indicate the positions of the maxima, and it can be seen that these are slightly elevated when a new vortex enters the field.

In order to compare the results regarding the growth rate obtained from simulations and experiments for the superposed fields, v_{rms} data at $z = 1.3$ were extracted. The logarithmic growth rate of v_{rms} was calculated and is shown in Fig. 13. Also the theoretical curves from Fig. 8(a) are shown. It is again clear that DNS_R32 and EXP_rough follow the local theory data closely. Also, the other experimental and DNS cases correspond well within the linear region. The small growth rates of these cases are related to the many azimuthal wavenumbers present; representing to first order an average of the growth rates in the flow, not only the strongest mode, where the average takes into account the energy present in every mode. The wavy pattern for the DNS_R04 simulation can be shown to be related to the entry of new vortices.

In Fig. 14 the mean angles of the stationary vortices are shown at each radial position around the disk for both experiments and simulations, where the angle for each vortex was calculated in the same way as described in Section 3.1. In Eq. (11), β was set from experiments by counting the vortices around the disk, and from DNS by looking at the most energetic mode from the Fourier transform. Note that this gives a global measure of β although there are local variations. In Fig. 14 for the dashed line of DNS_R04, the angle jumps from the theoretical $\beta = 24$ line to the $\beta = 28$ line, and last down to the $\beta = 32$ line at $R = 430$ and 540, respectively. The positions of the jumps correspond to when a new vortex entered the simulation flow field adding four new vortices to the full disk field, as shown when counting the vortices in Fig. 9. DNS_R01 and DNS_R01r also show increases in the number of stationary vortices with increasing Reynolds number. However, in both cases, since new vortices entered into the flow domain one by one (not being constrained by the domain size by multiples of 4 or 32 etc.), the vortex angle changes smoothly across the β isolines with increasing R . This behaviour is also observed for EXP_clean.

4. Summary and conclusions

A comparison of disturbance characteristics obtained by local linear theory, experiments and DNS has been undertaken for the rotating-disk boundary-layer flow. The comparison was made for stationary vortices induced by surface roughnesses. Results from local linear theory were compared with linear data from experiments and DNS for the stationary Type-I crossflow disturbance. The results agreed for all three approaches both when restricting the analysis to only one azimuthal wavenumber ($\beta = 32$), and when allowing β to vary. This agreement clearly shows that the three approaches capture the same underlying physics, and lead to an accurate description of the flow. This agreement is of course expected, although one reason for its accuracy is the simplicity of the rotating-disk flow case when it comes to the setup and number of parameters that can vary, which is essentially only the edge Reynolds number. This makes the experiments very robust, accurate and repeatable compared with other flow cases (e.g. swept wing). Also, the local assumption of the linear theory is shown not to have a large impact when adjusting the flow to a global linear framework in DNS, in agreement with Refs. [17,18]. Further, the nonlinearities at large R in experiments do not influence the linear region for lower R . The results also verify the numerical simulations. The main aim of this paper was to show the agreement between theory, DNS and experiments, which has succeeded well. It can thus be argued that the case of the rotating disk is indeed a suitable flow case for theoretical, experimental and numerical work, as the various approaches can easily be compared with each other to high accuracy.

As noted in the introduction, the disturbance development in the rotating-disk boundary layer is also well known for the absolute instability that occurs above $R = 507$ [12,29]. However, in the present paper we focus on the linear development of stationary, convective disturbances at lower R and therefore interaction with the absolute instability is not relevant.

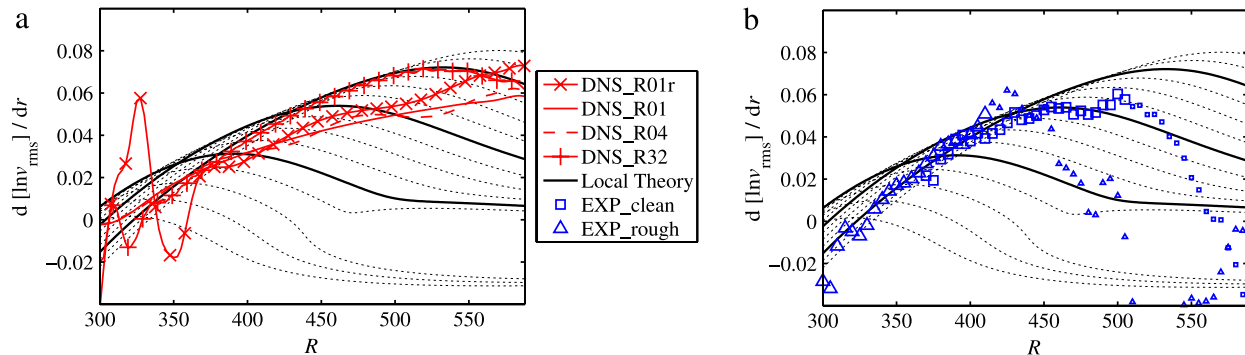


Fig. 13. Growth rate of the logarithmic v_{rms} in space of both DNS and experimental data, compared with $-\alpha_i$ from local theory where the curves are the same as in Fig. 8(a).

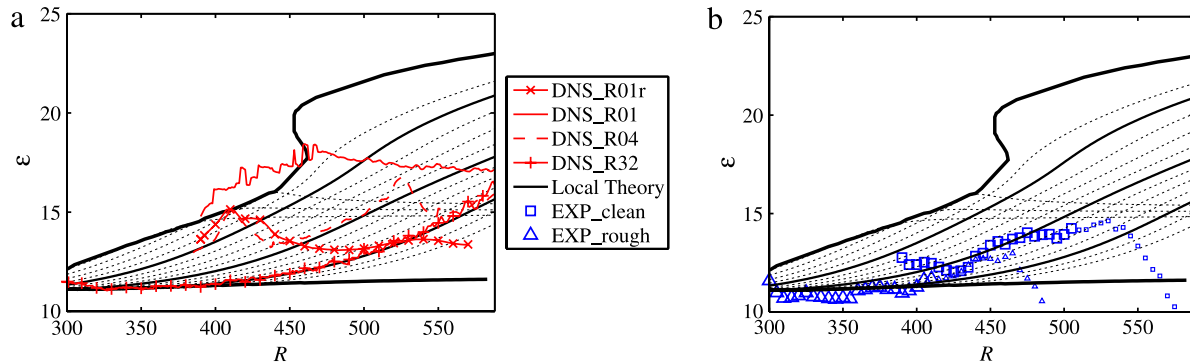


Fig. 14. Mean angle in degrees (ϵ) of both DNS and experimental data, compared with local theory where the curves are the same as in Fig. 8(b).

Acknowledgements

This work is supported by the Swedish Research Council through the ASTRID project 2013-5786 and from Linné FLOW Centre at KTH. Computer time was provided by the Swedish National Infrastructure for Computing (SNIC). Stimulating discussions with participants at the First Madingley Workshop, Cambridge, 23–25 July 2014 (Fluid Mechanics: an interdisciplinary approach) are warmly appreciated.

References

- [1] T. von Kármán, Über laminare und turbulent Reibung, *ZAMM Z. Angew. Math. Mech.* 1 (1921) 233–252.
- [2] E.D. Arco, E. Serre, P. Bontoux, *Stability, Transition and Turbulence in Rotating Cavities*, WIT Press, 2005.
- [3] N. Gregory, J.T. Stuart, W.S. Walker, On the stability of three-dimensional boundary layers with application to the flow due to a rotating disk, *Philos. Trans. R. Soc. Lond.* 248 (1955) 155–199.
- [4] R. Kobayashi, Y. Kohama, C. Takamadate, Spiral vortices in boundary layer transition regime on a rotating disk, *Acta Mech.* 35 (1980) 71–82.
- [5] S.P. Wilkinson, M.R. Malik, Stability experiments in the flow over a rotating disk, *AIAA J.* 23 (1985) 588–595.
- [6] S. Imayama, P.H. Alfredsson, R.J. Lingwood, On the laminar-turbulent transition of the rotating-disk flow: the role of absolute instability, *J. Fluid Mech.* 745 (2014) 132–163.
- [7] M.R. Malik, The neutral curve for stationary disturbances in rotating-disk flow, *J. Fluid Mech.* 164 (1986) 275–287.
- [8] R.J. Lingwood, *Stability and Transition of the Boundary Layer on a Rotating Disk* (Ph.D. thesis), Cambridge University, 1995.
- [9] M.R. Malik, S.P. Wilkinson, S.A. Orszag, Instability and transition in rotating disk flow, *AIAA J.* 19 (1981) 1131–1138.
- [10] L.M. Mack, The wave pattern produced by a point source on a rotating disk, *AIAA Paper-85-0490*, 1985.
- [11] A.J. Faller, Instability and transition of disturbed flow over a rotating disk, *J. Fluid Mech.* 230 (1991) 245.
- [12] R.J. Lingwood, Absolute instability of the boundary layer on a rotating disk, *J. Fluid Mech.* 299 (1995) 17–33.
- [13] Z. Hussain, S.J. Garrett, S.O. Stephen, The instability of the boundary layer over a disk rotating in an enforced axial flow, *Phys. Fluids* 23 (2011) 114108.
- [14] R.J. Lingwood, Absolute instability of the Ekman layer and related rotating flows, *J. Fluid Mech.* 331 (1997) 405–428.
- [15] B. Pier, Finite-amplitude crossflow vortices, secondary instability and transition in the rotating-disk boundary layer, *J. Fluid Mech.* 487 (2003) 315–343.
- [16] C. Davies, P.W. Carpenter, A novel velocity-vorticity formulation of the Navier-Stokes equations with applications to boundary layer disturbance evolution, *J. Comput. Phys.* 172 (2001) 119–165.
- [17] M.R. Malik, P. Balakumar, Nonparallel stability of rotating disk flow using PSE, in: M.Y. Hussaini, A. Kumar, C.L. Streett (Eds.), *Instability, Transition & Turbulence*, Springer, 1992, pp. 168–180.
- [18] E. Appelquist, *Direct numerical simulations of the rotating-disk boundary-layer flow* (Licentiate thesis), Royal Institute of Technology, KTH Mechanics, ISBN: 978-91-7595-202-4, 2014.
- [19] P.F. Fischer, J.W. Lottes, S.G. Kerkemeier, Nek5000, 2012, Web page. <http://nek5000.mcs.anl.gov>.
- [20] A.T. Patera, A spectral element method for fluid dynamics: Laminar flow in a channel expansion, *J. Comput. Phys.* 54 (1984) 468–488.
- [21] Y. Maday, A.T. Patera, Spectral element methods for the incompressible Navier-Stokes equations, in: A.K. Noor, J.T. Oden (Eds.), *State-of-the-Art Surveys on Computational Mechanics*, The American Society of Mechanical Engineers, 1989.
- [22] L.-W. Ho, *A Legendre Spectral Element Method for Simulation of Incompressible Unsteady Viscous Free-Surface Flows* (Ph.D. thesis), Massachusetts Institute of Technology, 1989.
- [23] M.O. Deville, P.F. Fischer, E.H. Mund, *High-Order Methods for Incompressible Fluid Flow*, Cambridge University Press, 2002.
- [24] H.M. Tufo, P.F. Fischer, Fast parallel direct solvers for coarse grid problems, *J. Parallel Distrib. Comput.* 61 (2001) 151–177.
- [25] E. Appelquist, P. Schlatter, P.H. Alfredsson, R.J. Lingwood, Global linear instability of the rotating-disk flow investigated through simulations, *J. Fluid Mech.* 765 (2015) 612–631.
- [26] M. Chevalier, P. Schlatter, A. Lundbladh, D.S. Henningson, *SIMSON-A Pseudo-Spectral Solver for Incompressible Boundary Layer Flows*, Technical Report, Royal Institute of Technology, KTH Mechanics, SE-100 44 Stockholm, Sweden, 2007.
- [27] S. Imayama, P.H. Alfredsson, R.J. Lingwood, A new way to describe the transition characteristics of a rotating-disk boundary-layer flow, *Phys. Fluids* 24 (2012) 031701.
- [28] S. Imayama, P.H. Alfredsson, R.J. Lingwood, An experimental study of edge effects on rotating-disk transition, *J. Fluid Mech.* 716 (2013) 638–657.
- [29] R.J. Lingwood, An experimental study of absolute instability of the rotating-disk boundary-layer flow, *J. Fluid Mech.* 314 (1996) 373–405.